# Three-Dimensional Crystal Plasticity Finite Element Simulation of Hot Compressive Deformation Behaviors of 7075 Al Alloy

*Lei-Ting Li, Y.C. Lin, Ling Li, Lu-Ming Shen, and Dong-Xu Wen*

Three-dimensional crystal plasticity finite element (CPFE) method is used to investigate the hot compressive deformation behaviors of 7075 aluminum alloy. Based on the grain morphology and crystallographic texture of 7075 aluminum alloy, the microstructure-based representative volume element (RVE) model was established by the pole figure inversion approach. In order to study the macroscopic stress-strain response and microstructural evolution, the CPFE simulations are performed on the established microstructure-based RVE model. It is found that the simulated stress-strain curves and deformation texture well agree with the measured results of 7075 aluminum alloy. With the increasing deformation degree, the remained initial weak Goss texture component tends to be strong and stable, which may result in the steady flow stress. The grain orientation and grain misorientation have significant effects on the deformation heterogeneity during hot compressive deformation. In the rolling-normal plane, the continuity of strain and misorientation can maintain across the low-angle grain boundaries, while the discontinuity of strain and misorientation is observed at the high-angle grain boundaries. The simulated results demonstrate that the developed CPFE model can well describe the hot compressive deformation behaviors of 7075 aluminum alloy under elevated temperatures.

## 1. Introduction

In industry, simulating the hot-deformation behaviors of alloys is helpful to reduce cost and accelerate design process for the hot-forming processes, such as rolling, extrusion, and forging. In general, the thermomechanical deformation behaviors of alloys in the plastic deformation are complex (Ref 1, 2). The mechanical properties of products are determined by the microstructures which are significantly affected by the processing parameters (Ref 3, 4). The macroscopic response of polycrystalline materials under various loading conditions can be precisely predicted by some macroscale models (Ref 5-8). Among these models, the finite element method is the most popular tool used to study the plastic deformation and microstructural evolution of metals or alloys (Ref 2-6). Kang (Ref 9) proposed a visco-plastic constitutive model to study the ratcheting behaviors of U71Mn rail steel. Ashtiani et al. (Ref 10) utilized the finite element method to study the deformation heterogeneity and the microstructural evolution of

aluminum alloy during hot rolling. Lin et al. (Ref 11, 12) investigated the effects of strain rates on the strain/stress distribution and microstructural evolution in 42CrMo steel by the finite element method. Liu et al. (Ref 13) investigated the hot workability of AZ31B magnesium alloy by combining processing maps and finite element method.

Although the macroscale finite element method is capable of describing the plastic deformation and microstructural evolution of materials, the detailed microstructural features are not incorporated in the conventional finite element framework. The crystal plasticity (CP) model, which considers the dislocation slip and crystal rotation, has been widely used to simulate the heterogeneous plastic deformation (Ref 14-17) and texture evolution (Ref 18-20). The crystal plasticity finite element (CPFE) method is a powerful tool to study the plastic deformation of the polycrystalline materials. Recently, the representative volume element (RVE) model (Ref 21) has been developed to investigate the deformation heterogeneity of the polycrystalline material, and obtain the macroscopic response. In order to precisely represent the initial microstructure of materials, a number of microstructure-based RVE models have been established (Ref 16-21). Zhang et al. (Ref 22) developed a microstructure-based CP model to simulate the monotonic and cyclic deformation behaviors of Ti-6Al-4V alloy considering the distributions of orientation and misorientation. Kirane et al. (Ref 23) developed a three-dimensional (3D) microstructure-dependent CPFE model to investigate the fatigue crack nucleation behavior for polycrystalline Ti-6242. Zhang et al. (Ref 24) established a 3D polycrystalline microstructure-sensitive CP model to study the fretting fatigue behavior of Ti-6Al-4V alloy. Ramazani et al. (Ref 25) evaluated the flow curves of DP steels using 2D and 3D microstructure-based RVE models. Thomas et al. (Ref 26) developed an image-based CPFE approach to study the microstructure-dependent

**Lei-Ting Li, Y.C. Lin,** and **Dong-Xu Wen**, School of Mechanical and Electrical Engineering,Central South University, Changsha 410083, China and State Key Laboratory of High Performance Complex Manufacturing, Changsha 410083, China; and **Ling Li** and **Lu-Ming Shen**, School of Civil Engineering, The University of Sydney, Sydney, NSW 2006, Australia.Contact e-mails: yclin@csu.edu.cn and linyongcheng@163.com.

properties of Ti-6Al-4V alloy. Shin et al. (Ref 27) used a resolved shear stress criterion and the microstructure-based CPFE method to investigate the activation of twin variants in extruded AZ31 Mg alloy.

Due to their optimal physical and mechanical properties, Al-Zn-Mg-Cu alloys are primarily developed for aerospace vehicles structures (Ref 28-30). 7075 aluminum alloy is one of typical Al-Zn-Mg-Cu alloys. Up to now, some investigations have been carried out to study the relationships between the external conditions, microstructural evolution, and the mechanical properties of 7075 aluminum alloy (Ref 30-46). In order to accurately predict the flow stress of 7075 aluminum alloy under hot compression or tension loadings, some suitable constitutive models were developed by Lin et al. (Ref 31, 32), Rokni et al. (Ref 33), Quan et al. (Ref 34), Naser and Krallics (Ref 35), Paturi et al. (Ref 36), Zhou et al. (Ref 37), Zhang et al. (Ref 38), and Jenab et al. (Ref 39). Meanwhile, the microstructural evolution and high-temperature behaviors of 7075 aluminum alloy have been comprehensively investigated to optimize the forming processes (Ref 30, 40). Rajamuthamilselvan and Ramanathan (Ref 41), Jenab and Taheri (Ref 42), and Lin et al. (Ref 43) established the processing maps to study the flow behavior and microstructural evolution of 7075 aluminum alloy, and the optimal hot working parameters were identified. In addition, effects of creep aging on the precipitates' hardening behaviors and the corrosion resistance of 7075 aluminum alloy have been discussed elsewhere (Ref 44-46).

Although some investigations have been conducted to study the hot-deformation behaviors of 7075 aluminum alloy, the deformation heterogeneity and microstructural evolution during hot-compressive deformation still need to be further investigated. In this study, a microstructure-based RVE model is created using a 3D Voronoi tessellation method. Based on the established RVE model, a thermomechanical-coupled CP model is implemented into finite element method to investigate the deformation heterogeneity and microstructural evolution of 7075 aluminum alloy under elevated temperatures. The effects of grain misorientation on the strain and misorientation distributions are investigated in detail. The simulated results are validated by experiments.

## 2. Material and Experiments

The commercial 7075 aluminum alloy was used in this study, and the chemical compositions (wt.%) are as follows: 5.8Zn-2.3Mg-1.5Cu-0.16Fe-0.05Mn-0.02Ti-0.07Si-(bal.)Al. Cylindrical specimens with the diameter of 10 mm and the height of 12 mm were machined from the rolled alloy sheet. In order to reduce the friction between the specimen and dies during the hot compression, the end faces of specimens were recessed to a depth of 0.1 mm to contain the lubricant of mixture of graphite and machine oil. Hot-compression tests were conducted on a Gleeble-1500 thermosimulation machine. Two strain rates (0.01 and 0.1 s$^{-1}$) and three deformation temperatures (623, 673 and 723 K) were used in hot-compression tests, and the final deformation degree was 60%.

The EBSD system coupled with a Zeiss ULTRA plus scanning electron microscope (SEM) was applied in order to obtain the grain morphology and crystallographic orientation of 7075 aluminum alloy. Since the grain size of 7075 aluminum alloy is relative large, the scan step is chosen to be 2 μm. The rolling-transverse (R-T) and rolling-normal (R-N) planes of specimens were scanned, and the experimental results are shown in Fig. 1. The grain size of 7075 aluminum alloy can be determined as 500 μm × 250 μm × 50 μm from the inverse pole figure maps.

## 3. Establishment of Thermomechanical-Coupled Crystal Plasticity Model

Based on the work of Marin (Ref 47), the framework of thermomechanical-coupled CP constitutive model is established to describe the hot-compressive deformation behaviors of 7075 aluminum alloy. The key equations of thermomechanical-coupled CP constitutive model are summarized as follows.

Under the framework of the CP theory, the total deformation gradient **F** can be expressed as the multiplication of the elastic part: $F_e$ and the plasticity part: $F_p$, as shown in Eq. (1).

$$\mathbf{F} = F_e F_p \tag{Eq 1}$$

where $F_p$ represents the crystallographic slip along slip planes, and $F_e$ is the elastic deformation gradient incorporating the elastic stretch and rigid body rotation of the configuration.

The Green elastic strain defined in the relaxed configuration is given by

$$E_e = \frac{1}{2}\left[(F_e)^T F_e - \mathbf{I}\right] \tag{Eq 2}$$

where **I** is the second-order identity tensor. $\sigma_{con}$ is the conjugate stress, which can be expressed by

$$\sigma_{con} = \det F^e (F^e)^{-1} \sigma (F^e)^{-T} \tag{Eq 3}$$

where $\sigma$ is the Cauchy stress.

The plastic velocity gradient $L_p$ is expressed as

$$L_p = \dot{F}_p F_p^{-1} = \sum_{\alpha=1}^{N} \dot{\gamma}^{\alpha}(s^{\alpha} \otimes n^{\alpha}) \tag{Eq 4}$$

where $N$ is the total number of slip system, $\dot{\gamma}^{\alpha}$ is the shear strain rate on the $\alpha$-slip system, $s^{\alpha}$ is the slip direction, $n^{\alpha}$ is the orthogonal plane of $s^{\alpha}$, and $\otimes$ is the dyadic product.

However, the thermomechanical-coupled behaviors have significant effects on the flow stress during the hot compression. Therefore, in order to simulate the thermomechanical-coupled behaviors of 7075 aluminum alloy during hot compression, a thermal-activation hardening rule is used in this study. The shear strain rate on a slip system is assumed to be related to the resolved shear stress (defined as $\tau^{\alpha} = \sigma_{con} \cdot (s^{\alpha} \otimes n^{\alpha})$) and deformation temperature, i.e.,

$$\dot{\gamma}^{\alpha} = \dot{\gamma}_0 \left(\frac{|\tau^{\alpha}|}{h^{\alpha}}\right)^{1/m} \exp\left(-\frac{Q}{k_B T}\right) \text{sign}(\tau^{\alpha}) \tag{Eq 5}$$

where $\dot{\gamma}_0$ is the reference shear strain rate, $\tau^{\alpha}$ is the resolved shear stress on $\alpha$-slip system, $h^{\alpha}$ is the slip resistance of the $\alpha$-slip system, m is the strain rate sensitivity, $Q$ is the activation free energy, $k_B$ is the Boltzmann constant, and $T$ is the absolute temperature. The slip resistance on all the slip systems is given below:
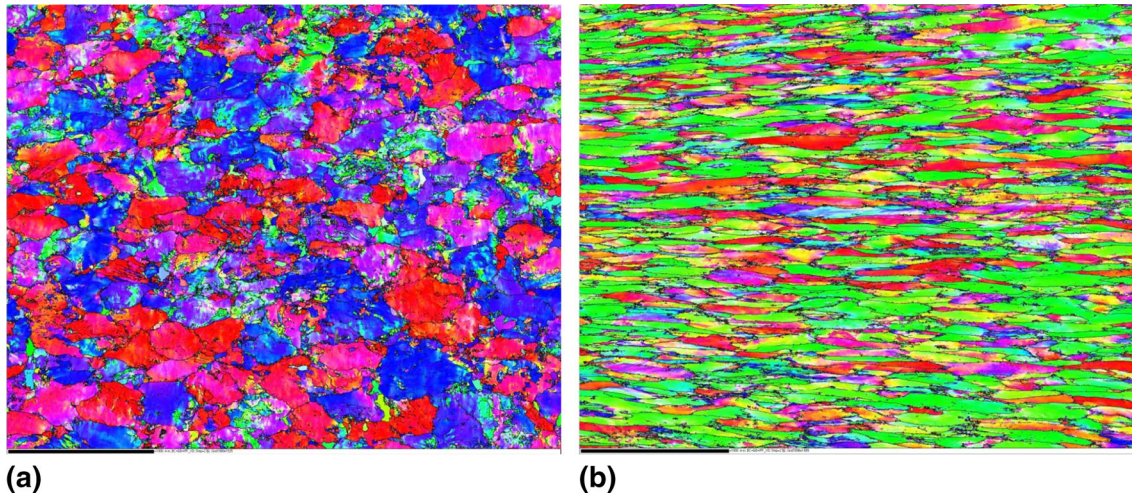
**Fig. 1** Initial microstructures of 7075 aluminum alloy in (a) rolling-transverse (R-T) plane and (b) rolling-normal (R-N) plane

$$h = \zeta_0 \left( \frac{h_s - h}{h_s - h_0} \right) \sum_{\alpha=1}^{N} |\dot{\gamma}^{\alpha}| \qquad \text{(Eq 6)}$$

where $\zeta_0$ is the initial hardening coefficient. $h_s$ and $h_0$ are the saturated and initial hardening strengths, respectively. $h_s$ is temperature dependent and can be computed through

$$h_s = h_{s0} \left( \frac{\sum_{\alpha=1}^{N} \dot{\gamma}^{\alpha}}{\dot{\gamma}_{s0}} \right)^{k_B T / A} \qquad \text{(Eq 7)}$$

where $h_{s0}$ represents the initial saturated hardening strength, $\dot{\gamma}_{s0}$ and A are material parameters.

In the hot-forming process, part of the plastic dissipation is generally converted into the heat which will result in the rise of deformation temperature. This energy conversion can be expressed as

$$\rho c \dot{T} = \chi \sum_{\alpha=1}^{N} \tau^{\alpha} \dot{\gamma}^{\alpha} \qquad \text{(Eq 8)}$$

where $\dot{T}$ is the temperature increase rate, $\rho$ is the mass density, $c$ is the specific heat capacity, and $\chi$ is the energy conversion efficiency.

The thermomechanical-coupled CP model is numerically implemented into ABAQUS standard solver (Ref 48) through user-defined material subroutine (UMAT) and user-defined material's thermal behavior subroutine (UMATHT).

## 4. Establishment of the Microstructure-Based RVE Model

Although the computational efficiency of computers has been increased tremendously, it is still a challenge to simulate the response of bulk material using CP model. In order to obtain the macroscopic response using CP model, a unit cell consisting of a number of grains is proposed to represent the initial microstructure statistically. Each grain will be discretized

further by the finite element mesh. In this study, the unit cell is a 3D RVE model which is built using a Voronoi tessellation technique (Ref 21).

However, too many grains in RVE model will reduce the efficiency of simulation. Therefore, using a minimum number of grains to represent the initial microstructure of materials is an efficient way. In general, in order to precisely represent the initial microstructure of alloys, sufficient grain orientations should be extracted from EBSD experiments, and assigned to each element of RVE model. However, extracting the sufficient grain orientations from the EBSD data is difficult since the mathematical and computational determination of the orientation density function (ODF) from diffraction pole figures is still a challenge. Raabe and Roters (Ref 49) used the texture-component approach to extract texture information from the experiment by reproducing the ODF, and then map the extracted texture information onto finite element grids for CP simulation. In the current research, a pole figure inversion approach proposed by Hielscher and Schaeben (Ref 50) is used to give a least-squares (LS) estimator of the unknown ODF. The weighted LS estimator is expressed as

$$f_{LS} = \arg\min \sum_{i=1}^{N} \sum_{j=1}^{N_i} I_{ij}^{-1} \left[ v_i \Re f (H_i, \mathbf{r}_{ij}) + I_{ij}^b - I_{ij} \right]^2 \qquad \text{(Eq 9)}$$

where $f_{LS}$ is the LS estimated ODF, $N$ is the number of pole figures, $N_i$ is the dimension of specimen, $I_{ij}$ is the diffraction counts, $v_i$ is the unknown normalisation factor, $\Re f(x)$ is an integral operator of $f(x)$, $H_i$ is the lattice planes, $\mathbf{r}_{ij}$ is the coordinate vector, and $I_{ij}^b$ is the background radiation.

Using the pole figure inversion approach, a given number of grain orientations can be uniquely generated by discretizing the ODF which is generated using the LS estimator. The pole figure inversion algorithm has been implemented as part of the texture analysis toolbox MTEX (Ref 50). Through the MATALAB toolbox MTEX, a numerical method was proposed to extract the given number of grains from EBSD data (Ref 51). In the grain orientation extraction process, the EBSD data obtained from the 7075 aluminum alloy specimen are imported to the toolbox MTEX, and then a given number of grain orientations are obtained by discretizing the ODF. In this study, 512, 729, 1000, and 1331 grain orientations are separately extracted from the

EBSD data for the convergence study of the microstructure-based RVE model. Figure 2 shows the pole figures from the experimental results, and the pole figures of the extracted grain orientations from EBSD data are shown in Fig. 3. From Fig. 3, it can be found that the extracted pole figures with 512 and 729 grain orientations cannot well capture the feature of the experimental pole figures. When the number of grain orientations is increased to 1000, the difference between the extracted and experimental pole figures is reduced. However, with the further increase of grain orientations, the extraction accuracy cannot be obviously improved. The number of grain orientations in the RVE model can be determined by the convergence study.

In order to determine the optimal numbers of grain and element of RVE model, convergence studies have been carried out. Figure 4(a) shows the effects of grain number on the convergence of flow stress. From Fig. 4(a), it can be found that the flow stress curves become converged when the grain number is 1000. With the continuous increase of grain, the prediction accuracy cannot be improved. Therefore, 1000 grains are used to establish the microstructure-based RVE model for 7075 aluminum alloy. After the optimal grain number of RVE model is determined, the convergence study of elements is performed on the RVE model with 1000 grains, as shown in Fig. 4(b). Considering the accuracy and computational efficiency, the RVE model with 108000 elements is adopted. From the above analysis, it can be confirmed that the established RVE model with 1000 grains discretized by 108000 elements is suitable for simulating the true stress-true strain curves for 7075 aluminum alloy. The microstructure-based RVE model for 7075 aluminum alloy is shown in Fig. 5. Periodic boundary conditions are applied in x, y, and z directions of the RVE model which would be compressed in z-direction.

# 5. Results and Discussion

## 5.1 Thermomechanical-Coupled Deformation Behavior of 7075 Aluminum Alloy

In this study, a thermomechanical-coupled CP model is implemented into finite element method to describe the hot compressive-deformation behaviors of 7075 aluminum alloy. The parameters used in the CPFE simulations are shown in Tables 1 and 2 (Ref 52). As shown in Eq 8, the resolved shear stress multiplied by shear strain rate results in the plastic dissipation during hot-compressive deformation. In general, part of the plastic dissipation can be converted into heat, which easily

leads to the rise of deformation temperature. The effects of temperature on the hot-deformation behaviors can be described by Eq 5-7. In order to study the thermomechanical-coupled behaviors using the finite element method, the plastic dissipation and the CP model were implemented by the subroutines UMATHT and UMAT, respectively. Through the UMAT and UMATHT subroutines, the thermomechanical-coupled deformation behaviors of 7075 aluminum alloy are investigated by the proposed CPFE model. Figure 6 compares the simulated results by the thermomechanical-coupled CP model with the experimental results. Obviously, the simulated true stress-true strain curves well correlates with the experimental result over wide strain range. It confirms that the thermomechanical-coupled microstructure-dependent CPFE model can give a precise prediction of the hot-compressive deformation behaviors of 7075 aluminum alloy. In addition, Fig. 6 indicates that the flow stress increases with the decrease of deformation temperature or the increase of strain rate. The flow stress increases to the peak stress sharply at a small strain, after which the flow stresses decrease monotonically until reaching high strains, showing a dynamic softening (Ref 53, 54).

## 5.2 Texture Evolution During the Hot Compressive Deformation

Maurice and Driver (Ref 55) found that aluminum can slip on $\{111\}\langle110\rangle$ and $\{110\}\langle110\rangle$ glide systems during hot rolling. Raabe (Ref 56) simulated the effects of $\{111\}\langle110\rangle$ and $\{110\}\langle110\rangle$ slip systems on the aluminum texture evolution during hot rolling, and found that activation of $\{110\}\langle110\rangle$ slip system significantly influences the evolution of Cube and Brass texture components, but slight effects on other texture components. Therefore, in this study, only $\{111\}\langle110\rangle$ slip systems are considered to investigate the texture evolution in 7075 aluminum alloy during hot deformation, and the evolution of Goss texture component is presented. Previously, Raabe (Ref 57) and Raabe and Becker (Ref 58) used the CPFE model was to calculate the microtexture and stored energy which were translated into cellular automation for the simulation of primary static recrystallization. Moreover, Raabe et al. (Ref 59) found that the influence of grain neighborhood interaction on the evolution of global texture was significant. In the current research, the texture evolution in 7075 aluminum alloy during hot deformation is simulated by CPFE model. Since the dynamic recrystallization can result in flow softening, a thermomechanical-coupled hardening rule is used to simulate the flow softening caused by the dynamic recrystallization
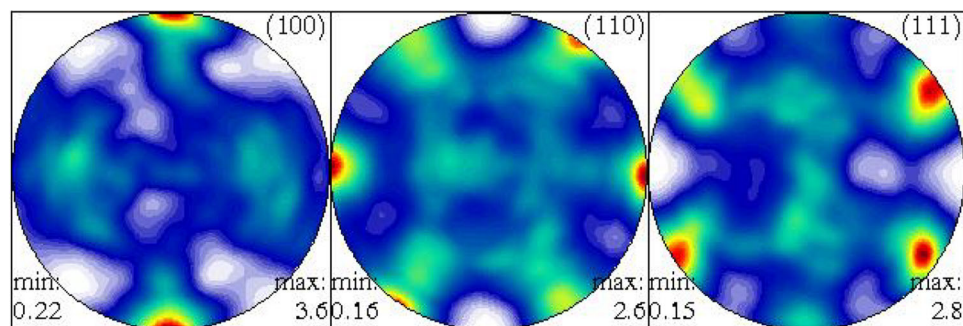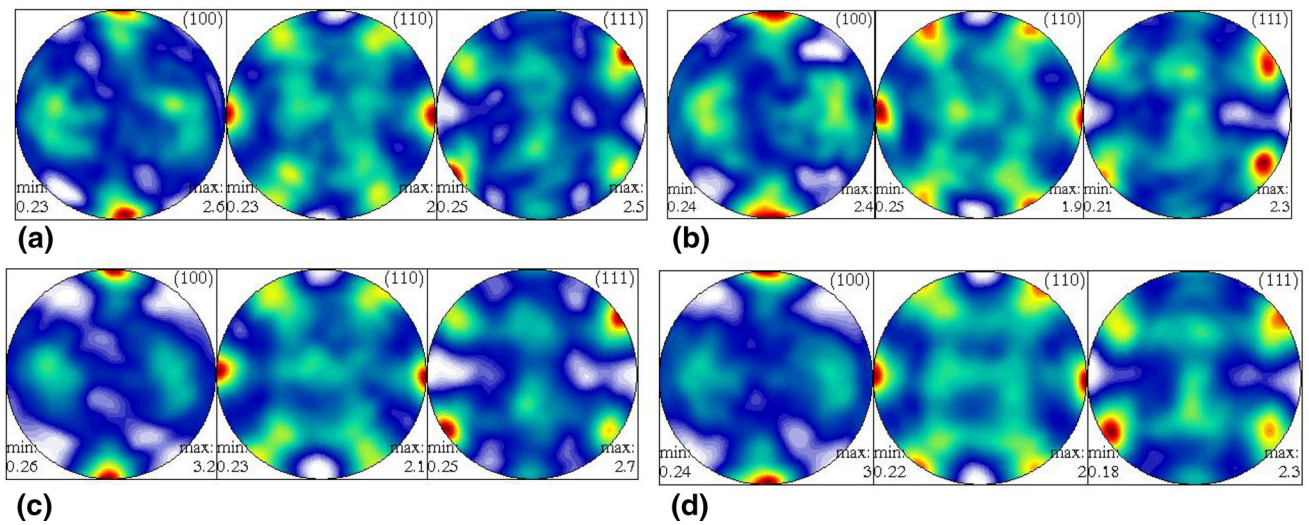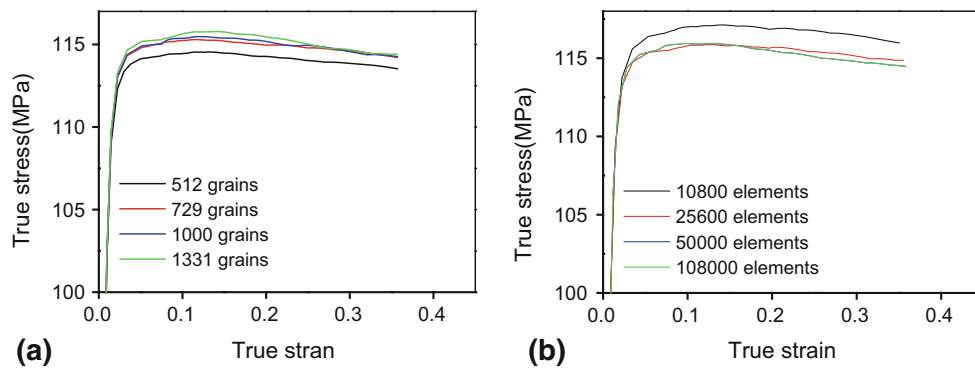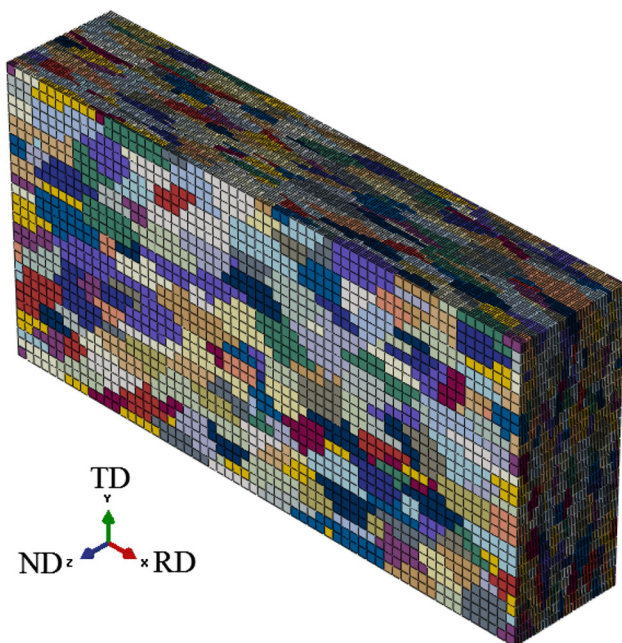


**Fig. 2** Pole figure of 7075 aluminum alloy obtained by EBSD experiments

**Fig. 3** Pole figures of 7075 aluminum alloy extracted from experimental results with grain orientation numbers of: (a) 512; (b) 729; (c) 1000; (d) 1331



**Fig. 4** True stress-strain curves of RVE models with (a) different numbers of grains; (b) 1000 grains discretized with different element numbers



**Fig. 5** RVE model for 7075 aluminum alloy

during hot deformation. Therefore, a 3D RVE model consisting of sufficient grains and elements are used to simulate the texture evolution in 7075 aluminum alloy during hot deformation.

In order to further verify the developed microstructure-dependent CPFE model, the simulated and measured pole figures have been compared in Fig. 7. From Fig. 7, it can be found that the proposed CPFE model can well capture the main texture features of 7075 aluminum alloy after hot-compressive deformation. It confirms that the microstructure-dependent CPFE model can not only predict the macroscopic tress-strain curves, but also simulate the texture evolution of 7075 aluminum alloy during the hot compressive deformation.

The texture evolution predicted by the microstructure-dependent CPFE model is shown in Fig. 8. The grain orientations in RVE model are plotted in {111} pole figure and inverse pole figure. Figure 8(a) represents the initial texture, while the deformed textures are shown in Fig. 8(b) and (c). From Fig. 8(a), it can be seen that the dominant grain orientation is close to the Goss orientation ( {110}⟨001⟩) which is weak in the as-received 7075 aluminum alloy. It is well known that the Goss orientation is a typical recrystallization texture in aluminum alloys. This indicates that few recrystallization grains exist in the microstructure of as-received 7075

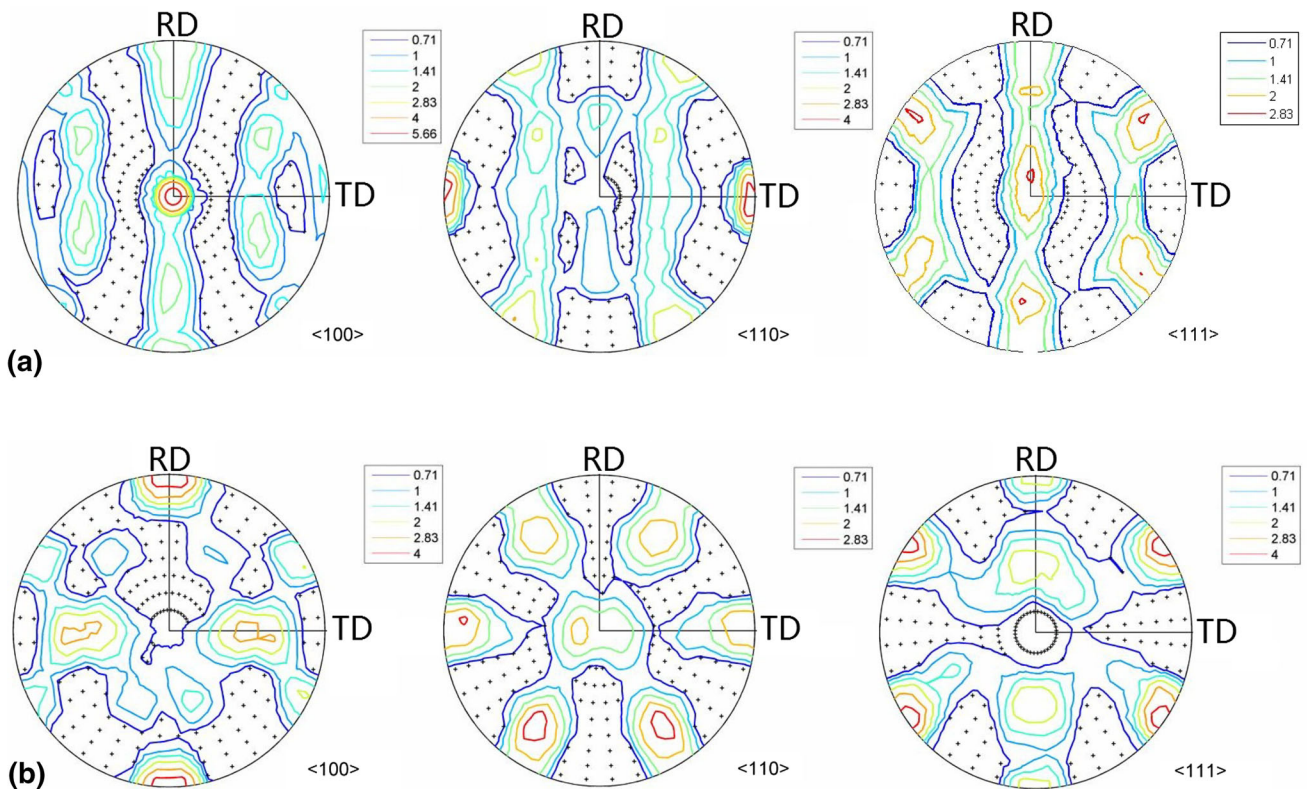**Table 1  Material parameters of the developed CP model for 7075 aluminum alloy**

| $\zeta_0$, MPa | $h_0$, MPa | $h_{s0}$, MPa | $\dot{\gamma}_{s0}$, s$^{-1}$ |
|---|---|---|---|
| 22.4 | 43.2 | 43.2 | $5 \times 10^{10}$ |

**Table 2  Material parameters for the thermal activation**

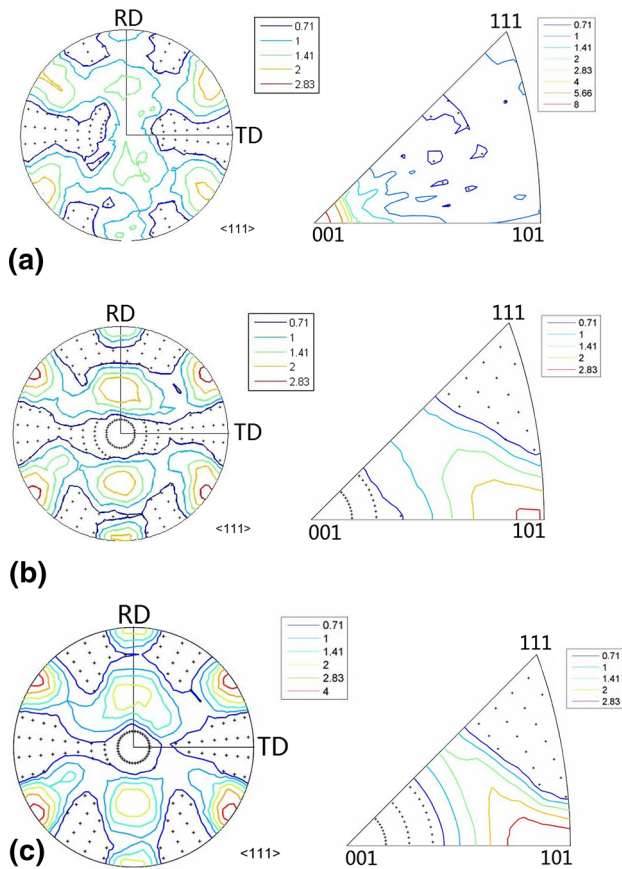| $Q$, J | $k_B$, J/K | $A$, J | $\rho$, kg/m$^3$ | $C$, J/kg K | $\chi$ |
|---|---|---|---|---|---|
| $3.0 \times 10^{-22}$ | $1.38 \times 10^{-23}$ | $1.86 \times 10^{-11}$ | 2800 | 960 | 0.9 |
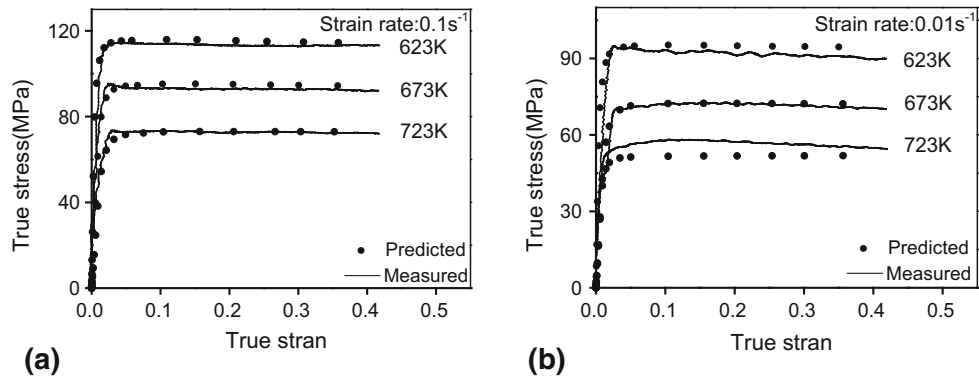


**Fig. 6**  Comparisons between the predicted and measured true strain-true stress curves at strain rates of (a) 0.1 s$^{-1}$; (b) 0.01 s$^{-1}$



**Fig. 7**  Pole figures of 7075 aluminum alloy (a) obtained by the EBSD experiment and (b) predicted by the microstructure-dependent CPFE model. (deformation degree: 60%, strain rate: 0.1 s$^{-1}$; deformation temperature: 623 K)

aluminum alloy. When the true strain is increased to 0.45, the texture component type is not altered, but the Goss component has been strong, as shown in Fig. 8(b). With the further
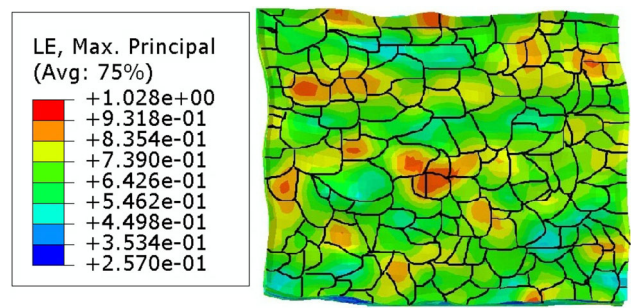
straining, the remained initial texture component tends to be stable. In general, the divergence behavior of the reorientation field for an orientation under the compressive load can be used

**Fig. 8** {111} and inverse pole figures of 7075 aluminum alloy at the true strains of: (a) 0; (b) 0.45; (c) 0.9



**Fig. 9** Strain field of 7075 aluminum alloy in the R-T plane. (strain rate: 0.1 s$^{-1}$; deformation temperature: 623 K)

### 5.3 Effects of Grain Orientation and Grain Boundary Misorientation on Strain Distribution

Figure 9 shows the effects of grain orientation and misorientation on the strain field of 7075 aluminum alloy at the deformation degree of 60% in the R-T plane. The grain boundaries are highlighted using black lines. It can be seen that the distribution of strain is inhomogeneous due to different grain orientations. The strain concentration appears at some grain boundaries, resulting in a strain discontinuity at these grain boundaries. However, there is strain continuity across some other grain boundaries. As Raabe figured out (Ref 67), the crystal kinematics significantly affects the strain heterogeneity between the neighbour grains. The grains with large strains are kinematically soft while the kinematically hard grains have small strains. During hot deformation, the strain path follows soft grains and avoids hard grains. However, the effects of the grain boundary misorientation on the strain distribution are not obvious in the R-T plane since the loading axial is perpendicular to the R-T plane.

Figure 10(a) shows the strain distribution of 7075 aluminum alloy at the deformation degree of 60% in the R-N plane. The inhomogeneous strain field can also be found. From Fig. 10(a), a narrow area with relatively large strain value is marked with a quadrangle. Figure 10(b-d) shows the evolution of strain field in the quadrangle with the increase of deformation degree. In the R-N plane, the evolution of the strain field at the grain boundary junction can be easily observed in Fig. 10(b-d). At the deformation degree of 47%, a small area (the red area shown in Fig. 10b) with relatively large strain value appears at the grain boundary junction. As the deformation proceeds, this small area becomes larger and grows from the grain boundary to the grain interior. When the deformation degree is increased to 60%, the strain field with relatively large strain value expands from one grain to the adjacent grains. At the beginning of the hot deformation, the deformation incompatibility appears at the junction of the grain boundaries, resulting in the strain concentration. With the increase of the deformation degree, the strain concentration expands to the grain interior. In general, strain localization at triple junctions is more obvious than that at straight grain boundaries. Similar results from CP simulations were reported by Raabe et al. (Ref 67). It was found that the triple junctions might be the nucleation sites for strain localization, and the grain boundary misorientation affects the strain heterogeneity. From Fig. 10(d), it can be seen that the strain field cannot go across the grain boundary between grains 1 and 2, while the strain field can expand from grain 1 to grain 3. The occurrence of this phenomenon is possibly induced by

to describe the tendency for orientation stability (Ref 60). The negative divergence of reorientation field controls the reorientation behavior of stable orientations. These orientations tend to be stable and orientation gradient is not prone to be built up. For example, the Goss texture component in face center cubic (FCC) crystals is one of the stable texture components under plane strain load (Ref 61). Therefore, after the compressive deformation, the unstable initial Goss texture has become fairly stable.

In addition, the dynamic recrystallization is prone to occur and considered as the preferred deformation mechanism to refine grain during the hot deformation (Ref 62-64). From the author's previous work (Ref 43), it can be found that the initial microstructure of 7075 aluminum alloy has been replaced by the recrystallized microstructures after the hot compressive deformation, resulting in a strong Goss texture component. Therefore, after the compressive deformation, the unstable initial Goss texture has become fairly stable due to the dynamic recrystallization. Eickemeyer et al. (Ref 65) studied the cold rolling behavior of Nickel, and found that the recrystallization cube texture tends to be stable with the further straining. Moreover, it was found that the unstable texture easily leads to the deformation shear bands during the plastic deformation (Ref 66). It can be concluded that the stable and strong Goss texture component may result in the stable flow during the hot compressive deformation of 7075 aluminum alloy, as shown in Fig. 6.
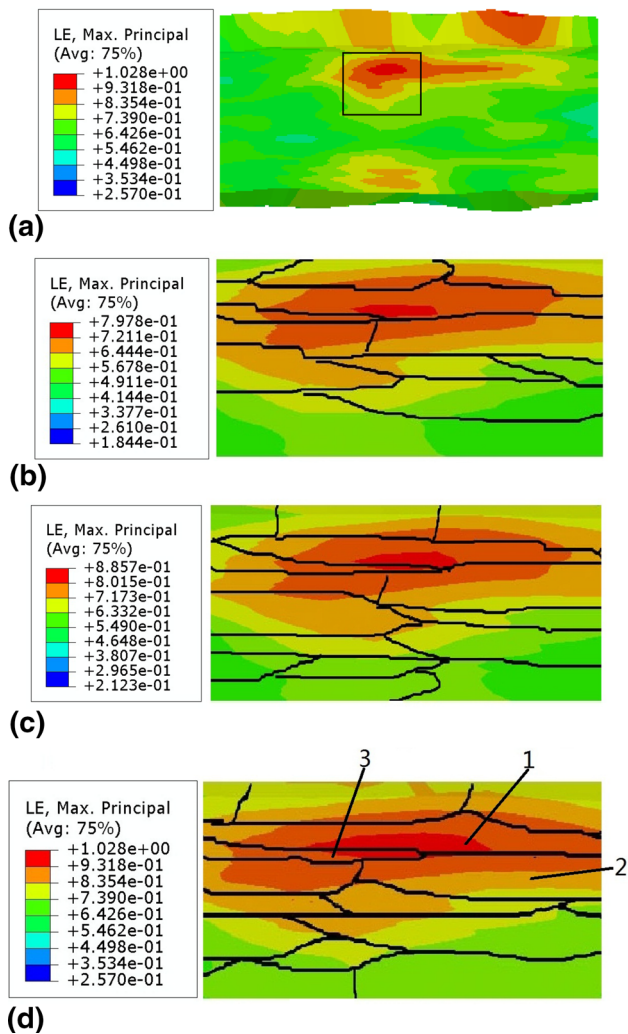
**Fig. 10** Strain distribution of 7075 aluminum alloy in the R-N plane. (a) after the deformation. The detailed track of the strain field in the quadrangle shown in (a) at the deformation degrees of (b) 47%; (c) 52%; (d) 60%

the grain boundary misorientation. The grain boundary angle between grains 1 and 2 is relatively high (36.02°), while that between grains 1 and 3 is a low-angle grain boundary (5.83°). It can be concluded that the strain field can go across the low-angle grain boundaries, while high-angle grain boundaries act as barriers in the R-N plane. Similar simulation results were observed by Sachtleber et al. (Ref 68), who found that the

maximum strain appears at high-angle grain boundaries while the effects of low-angle grain boundaries on strain distribution are less pronounced.

During hot deformation, the severely deformed regions have high stored energy. The nucleation of recrystallized grain is thermally activated process, and the driving force of nucleation is provided by the energy stored during hot deformation. However, the stored energy generated during hot deformation is too low to drive the homogeneous nucleation. Therefore, recrystallization nucleation usually occurs in the regions with local heterogeneities (Ref 69). As shown in Fig. 10, strain localization appears at the triple junction of grains 1, 2, and 3. This region with high strain amplitude may be the potential nucleation site for recrystallized grains.

Since the texture tends to be stable, Fig. 11 shows only the ⟨111⟩ pole figures of grains 1, 2, and 3 after the compressive compression. It can be found that the pole figures of grains 1 and 3 are almost the same, and different from that of grain 2. It reveals that the grain boundary between grains 1 and 2 is still a high-angle grain boundary, while that between grains 1 and 3 is a low-angle grain boundary. The initial orientation of each element in one grain is the same, and the texture shown in pole figure is concentrated. As can be seen from Fig. 11, the texture is divergent after the deformation, which indicates that the deformation heterogeneity occurs in every grain (shown in Fig. 10). Zhao et al. (Ref 70) also found that the strain heterogeneity is significantly affected by the microtexture through experiments and 3D CP simulations. This is due to the separation of in-grain kinematics and grain interaction, as discussed by Raabe et al. (Ref 67).

### 5.4 Effects of Grain Orientation and Grain Boundary Misorientation on Misorientation Distribution

In order to study the rotation of grain angle during hot-compressive deformation, the grain angle misorientation between the as-received and the deformed 7075 aluminum alloy for each element is also calculated. In the misorientation calculation process, the Euler angles are converted into the orientation matrix, and the misorientation matrix $A_{mis}$ can be evaluated from the initial and current orientations, as shown in Eq 10.
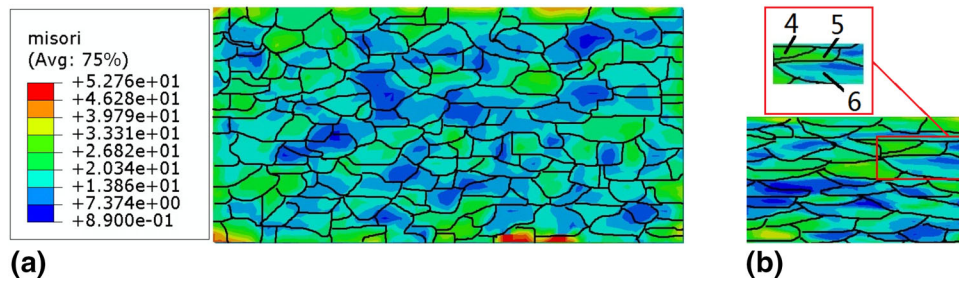
$$A_{mis} = M_2 M_1^{-1} \tag{Eq 10}$$

where $M_1$ and $M_2$ are the orientation matrices for the initial and current orientations, respectively. The misorientation $\Delta\Theta$ can be computed from the misorientation matrix $A_{mis}$, and $\Delta\Theta$ is formulated by Eq 11.
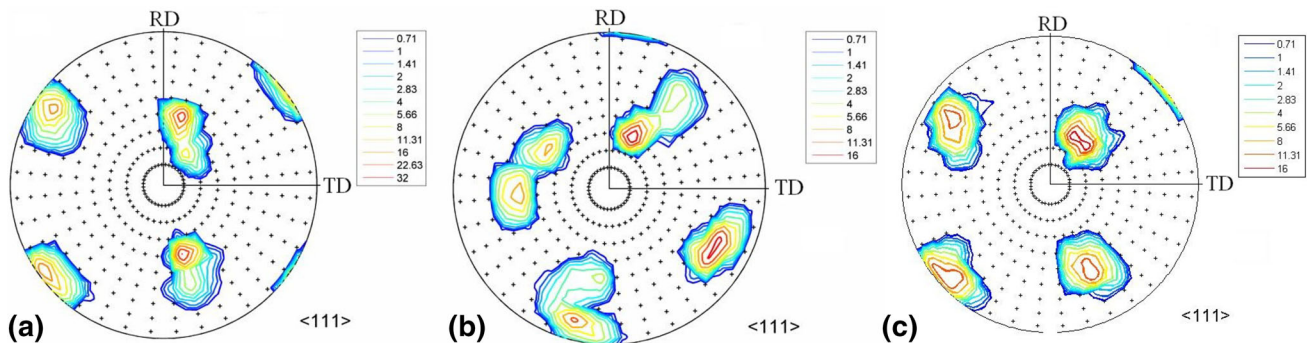


**Fig. 11** ⟨111⟩ pole figures of (a) grain 1, (b) grain 2, and (c) grain 3 after the hot deformation

**Fig. 12** The misorientation distributions of 7075 aluminum alloy in (a) R-T plane and (b) R-N plane

$$\Delta\Theta = \arccos\{[tr(\mathbf{A}_{\mathrm{mis}}) - 1]/2\} \qquad \text{(Eq 11)}$$

There are 24 crystallographically equivalent misorientations considering the symmetry of the FCC crystal. The minimum of all the misorientations is adopted as the final misorientation for each element.

Figure 12 shows the misorientation distribution of 7075 aluminum alloy after the hot deformation. The value of misorientation can be used to represent the rotation degree of each crystal. From Fig. 12, it can be found that the distribution of misorientation is inhomogeneous and the maximum misorientation angle is 52.76°. The maximum misorientation appears at the edges of the RVE model, and most of the misorientations are less than 30°. The relatively homogeneous distribution of misorientation within the grain is observed, and misorientation continuity or discontinuity at the grain boundaries can be found. Also, the effects of grain boundary on the misorientation distribution are obvious in the R-N plane. As shown in Fig. 12(b), the misorientation of the grain boundary between grains 4 and 5 is 6.26°, while that between grains 5 and 6 is 55.68°. It can also be concluded that the misorientation continuity is present across the low-angle grain boundary, while the misorientation discontinuity appears at the high-angle grain boundary. Therefore, it can be concluded that the grain rotation incompatibility can occur at the high-angle grain boundary, and the low-angle grain boundary has little effect on the misorientation distribution during the hot-compressive deformation.

## 6. Conclusions

The deformation heterogeneity and microstructural evolution of 7075 aluminum alloy during hot-compressive deformation are investigated by a 3D CPFE method. The simulated results show that the developed microstructure-based RVE model can well represent the grain morphology and crystallographic texture of 7075 aluminum alloy with the minimum number of grains. By performing the microstructure-dependent CPFE simulations, the macroscopic stress-strain curves and the deformation texture can be well predicted. After the hot-compressive deformation, the initial weak Goss texture component has been strong and tends to be stable with the further straining. The stable Goss texture is preferred in the metal forming and might result in the stable flow. The grain orientation and the misorientation have a significant effect on the deformation heterogeneity of 7075 aluminum alloy. In the R-N plane, the concentrations of strain and misorientation appear at high-angle grain boundaries, while the low-angle grain boundaries have little effect on the distributions of strain and misorientation.

## References

1. Y.C. Lin and X.M. Chen, A Critical Review of Experimental Results and Constitutive Descriptions for Metals and Alloys in Hot Working, *Mater. Des.*, 2011, **32**, p 1733–1759
2. D. Samantaray, S. Mandal, M. Jayalakshmi, C.N. Athreya, A.K. Bhaduri, and V.S. Sarma, New Insights into the Relationship Between Dynamic Softening Phenomena and Efficiency of Hot Working Domains of a Nitrogen Enhanced 316L(N) Stainless Steel, *Mater. Sci. Eng. A*, 2014, **598**, p 368–375
3. A. Łukaszek-Sołek and J. Krawczyk, The Analysis of the Hot Deformation Behaviour of the Ti-3Al-8V-6Cr-4Zr-4Mo Alloy, Using Processing Maps, A Map of Microstructure and of Hardness, *Mater. Des.*, 2015, **65**, p 165–173
4. B. Thossatheppitak, V. Uthaisangsuk, P. Mungsuntisuk, S. Suranuntchai, and A. Manonukul, Flow Behaviour of Nickel Aluminium Bronze Under Hot Deformation, *Mater. Sci. Eng. A*, 2014, **604**, p 183–190
5. S.V. Sajadifar and G.G. Yapici, Elevated Temperature Mechanical Behavior of Severely Deformed Titanium, *J. Mater. Eng. Perform.*, 2014, **23**, p 1834–1844
6. I. Balasundar, T. Raghu, and B.P. Kashyap, Modeling the Hot Working Behavior of Near-α Titanium Alloy IMI834, *Prog. Nat. Sci. Mater. Int.*, 2013, **23**, p 598–607
7. N. Kotkunde, A.D. Deole, A.K. Gupta, and S.K. Singh, Comparative Study of Constitutive Modeling for Ti-6Al-4V Alloy at Low Strain Rates and Elevated Temperatures, *Mater. Des.*, 2014, **55**, p 999–1005
8. N. Kotkunde, H.N. Krishnamurthy, P. Puranik, A.K. Gupta, and S.K. Singh, Microstructure Study and Constitutive Modeling of Ti-6Al-4V Alloy at Elevated Temperatures, *Mater. Des.*, 2014, **54**, p 96–103
9. G.Z. Kang, A Visco-Plastic Constitutive Model for Ratcheting of Cyclically Stable Materials and Its Finite Element Implementation, *Mech. Mater.*, 2004, **36**, p 299–312

10. H.R.R. Ashtiani, H. Bisadi, and M. Adabjou, Modeling of Microstructural Evolution During the Hot Rolling of Aluminum Alloy, *Int. Rev. Model. Simul.*, 2010, **3**, p 1129–1136

11. Y.C. Lin, M.S. Chen, and J. Zhong, Numerical Simulation for Stress/Strain Distribution and Microstructural Evolution in 42CrMo Steel During Hot Upsetting Process, *Comput. Mater. Sci.*, 2008, **43**, p 1117–1122

12. Y.C. Lin and M.S. Chen, Numerical Simulation and Experimental Verification of Microstructure Evolution in a 3-Dimensional Hot Upsetting Process, *J. Mater. Process. Technol.*, 2009, **209**, p 4578–4583

13. J. Liu, Z.S. Cui, and C.X. Li, Analysis of Metal Workability by Integration of FEM and 3-D Processing Maps, *J. Mater. Process. Technol.*, 2008, **205**, p 497–505

14. O. Diard, S. Leclercq, G. Rousselier, and G. Cailletaud, Evaluation of Finite Element Based Analysis of 3D Multicrystalline Aggregates Plasticity: Application to Crystal Plasticity Model Identification and the Study of Stress and Strain Fields Near Grain Boundaries, *Int. J. Plast.*, 2005, **21**, p 691–722

15. G.B. Sarma, B. Radhakrishnan, and T. Zacharia, Finite Element Simulations of Cold Deformation at the Mesoscale, *Comput. Mater. Sci.*, 1998, **12**, p 105–123

16. F. Roters, Application of Crystal Plasticity FEM from Single Crystal to Bulk Polycrystal, *Comput. Mater. Sci.*, 2005, **32**, p 509–517

17. S.Y. Li, B.R. Donohue, and S.R. Kalidindi, A Crystal Plasticity Finite Element Analysis of Cross-Grain Deformation Heterogeneity in Equal Channel Angular Extrusion and Its Implications for Texture Evolution, *Mater. Sci. Eng. A*, 2008, **480**, p 17–23

18. W.J. He, S.H. Zhang, A. Prakash, and D. Helm, A Hierarchical Multi-Scale Model for Hexagonal Materials Taking into Account Texture Evolution During Forming Simulation, *Comput. Mater. Sci.*, 2014, **82**, p 464–475

19. M. Liu, A.K. Tieu, C. Lu, Ht Zhu, and G.Y. Deng, A Crystal Plasticity Study of the Effect of Friction on the Evolution of Texture and Mechanical Behaviour in the Nano-Indentation of an Aluminium Single Crystal, *Comput. Mater. Sci.*, 2014, **81**, p 30–38

20. D.K. Kim, K.H. Jung, W.W. Park, Y.T. Im, and Y.S. Lee, Numerical Study of the Effect of Prior Deformation History on Texture Evolution during Equal Channel Angular Pressing, *Comput. Mater. Sci.*, 2014, **81**, p 68–78

21. R. Quey, P.R. Dawson, and F. Barbe, Large-Scale 3D Random Polycrystals for the Finite Element Method: Generation, Meshing and Remeshing, *Comput. Methods Appl. Mech. Eng.*, 2011, **200**, p 1729–1745

22. M. Zhang, J. Zhang, and D.L. McDowell, Microstructure-Based Crystal Plasticity Modeling of Cyclic Deformation of Ti-6Al-4V, *Int. J. Plast.*, 2007, **23**, p 1328–1348

23. K. Kirane and S. Ghosh, A Cold Dwell Fatigue Crack Nucleation Criterion for Polycrystalline Ti-6242 Using Grain-Level Crystal Plasticity FE Model, *Int. J. Fatigue*, 2008, **30**, p 2127–2139

24. M. Zhang, D.L. McDowell, and R.W. Neu, Microstructure Sensitivity of Fretting Fatigue Based on Computational Crystal Plasticity, *Tribol. Int.*, 2009, **42**, p 1286–1296

25. A. Ramazani, K. Mukherjee, H. Quade, U. Prahl, and W. Bleck, Correlation Between 2D and 3D Flow Curve Modelling of DP Steels Using a Microstructure-Based RVE Approach, *Mater. Sci. Eng. A*, 2013, **560**, p 129–139

26. J. Thomas, M. Groeber, and S. Ghosh, Image-Based Crystal Plasticity FE Framework for Microstructure Dependent Properties of Ti-6Al-4V Alloys, *Mater. Sci. Eng. A*, 2012, **553**, p 164–175

27. E.J. Shin, A. Jung, S.H. Choi, A.D. Rollett, and S.S. Park, A Theoretical Prediction of Twin Variants in Extruded AZ31 Mg Alloys Using the Microstructure Based Crystal Plasticity Finite Element Method, *Mater. Sci. Eng. A*, 2012, **538**, p 190–201

28. L. Chen, G.Q. Zhao, J.Q. Yu, and W.D. Zhang, Constitutive Analysis of Homogenized 7005 Aluminum Alloy at Evaluated Temperature for Extrusion Process, *Mater. Des.*, 2015, **66**, p 129–136

29. C.J. Shi, W.M. Mao, and X.G. Chen, Evolution of Activation Eenergy During Hot Deformation of AA7150 Aluminum Alloy, *Mater. Sci. Eng. A*, 2013, **571**, p 83–91

30. W.T. Huo, L.G. Hou, H. Cui, L.Z. Zhuang, and J.S. Zhang, Fine-Grained AA 7075 Processed by Different Thermo-mechanical Processing, *Mater. Sci. Eng. A*, 2014, **618**, p 244–253

31. Y.C. Lin, L.T. Li, and Y.Q. Jiang, A Phenomenological Constitutive Model for Describing Thermo-viscoplastic Behavior of Al-Zn-Mg-Cu Alloy Under Hot Working Condition, *Exp. Mech.*, 2012, **52**, p 993–1002

32. Y.C. Lin, L.T. Li, Y.X. Fu, and Y.Q. Jiang, Hot Compressive Deformation Behavior of 7075 Al Alloy Under Elevated Temperature, *J. Mater. Sci.*, 2012, **47**, p 1306–1318

33. M.R. Rokni, A. Zarei-Hanzaki, C.A. Widener, and P. Changizian, The Strain-Compensated Constitutive Equation for High Temperature Flow Behavior of an Al-Zn-Mg-Cu Alloy, *J. Mater. Eng. Perform.*, 2014, **23**, p 4002–4009

34. G.Z. Quan, G.S. Li, Y. Wang, W.Q. Lv, C.T. Yu, and J. Zhou, A Characterization for the Flow Behavior of As-Extruded 7075 Aluminum Alloy by the Improved Arrhenius Model with Variable Parameters, *Mater. Res.*, 2013, **16**, p 19–27

35. T.S.B. Naser and G. Krallics, Mechanical Behavior of Multiple-Forged Al 7075 Aluminum Alloy, *Acta Polytech. Hung.*, 2014, **11**, p 103–117

36. U.M.R. Paturi, S.K.R. Narala, and R.S. Pundir, Constitutive Flow Stress Formulation, Model Validation and FE Cutting Simulation for AA7075-T6 Aluminum Alloy, *Mater. Sci. Eng. A*, 2014, **605**, p 176–185

37. M. Zhou, Y.C. Lin, J. Deng, and Y.Q. Jiang, Hot Tensile Deformation Behaviors and Constitutive Model of an Al-Zn-Mg-Cu Alloy, *Mater. Des.*, 2014, **59**, p 141–150

38. D.N. Zhang, Q.Q. Shangguan, C.J. Xie, and F. Liu, A Modified Johnson-Cook Model of Dynamic Tensile Behaviors for 7075-T6 Aluminum Alloy, *J. Alloy. Compd.*, 2015, **619**, p 186–194

39. A. Jenab, A.K. Taheri, and K. Jenab, The Use of ANN to Predict the Hot Deformation Behavior of AA7075 at Low Strain Rates, *J. Mater. Eng. Perform.*, 2013, **22**, p 903–910

40. M.R. Selvan and S. Ramanathan, Effect of Silicon Carbide Volume Fraction on the Hot Workability of 7075 Aluminium-Based Metal-Matrix Composites, *Int. J. Adv. Manuf. Technol.*, 2013, **67**, p 1711–1720

41. M. Rajamuthamilselvan and S. Ramanathan, Hot Deformation Behaviour of 7075 Alloy, *J. Alloy. Compd.*, 2011, **509**, p 948–952

42. A. Jenab and A.K. Taheri, Experimental Investigation of the Hot Deformation Behavior of AA7075: Development and Comparison of Flow Localization Parameter and Dynamic Material Model Processing Maps, *Int. J. Mech. Sci.*, 2014, **78**, p 97–105

43. Y.C. Lin, L.T. Li, Y.C. Xia, and Y.Q. Jiang, Hot Deformation and Processing Map of a Typical Al-Zn-Mg-Cu Alloy, *J. Alloy. Compd.*, 2013, **550**, p 438–445

44. Y.C. Lin, Y.Q. Jiang, X.M. Chen, D.X. Wen, and H.M. Zhou, Effect of Creep-Aging on the Precipitates of 7075 Aluminum Alloy, *Mater. Sci. Eng. A*, 2013, **588**, p 347–356

45. L.T. Li, Y.C. Lin, H.M. Zhou, Y.C. Xia, and Y.Q. Jiang, Modeling the High-Temperature Creep Behaviors of 7075 and 2124 Aluminum Alloys by Continuum Damage Mechanics Model, *Comput. Mater. Sci.*, 2013, **73**, p 72–78

46. Y.C. Lin, Y.Q. Jiang, X.C. Zhang, J. Deng, and X.M. Chen, Effect of Creep-Aging Processing on Corrosion Resistance of an Al-Zn-Mg-Cu Alloy, *Mater. Des.*, 2014, **61**, p 228–238

47. E.B. Marin, Sandia National Laboratories, 2006

48. ABAQUS, Hibbit, Karlsson and Sorensen Inc., 2011

49. D. Raabe and F. Roters, Using Texture Components in Crystal Plasticity Finite Element Simulations, *Int. J. Plast.*, 2004, **20**, p 339–361

50. R. Hielscher and H. Schaeben, A Novel Pole Figure Inversion Method: Specification of the MTEX Algorithm, *J. Appl. Cryst.*, 2008, **41**, p 1024–1037

51. L. Li, L.M. Shen, and G. Proust, A Texture-Based Representative Volume Element Crystal Plasticity Model for Predicting Bauschinger Effect during Cyclic Loading, *Mater. Sci. Eng. A*, 2014, **608**, p 174–183

52. L.T. Li, Y.C. Lin, L. Li, and L.M. Shen, Finite Element Simulation of the Hot Deformation Behavior of AA7075 Using a Coupled Thermo-Mechanical Crystal Plasticity Constitutive Model, *Appl. Mech. Mater.*, 2014, **553**, p 82–87

53. H. Mirzadeh, M.H. Parsa, and D. Ohadi, Hot Deformation Behavior of Austenitic Stainless Steel for a Wide Range of Initial Grain Size, *Mater. Sci. Eng. A*, 2013, **569**, p 54–60

54. S.V. Sajadifar, M. Ketabchi, and M. Nourani, Modeling of Mechanical Characteristics in Hot Deformation of 4130 Steel, *Steel Res. Int.*, 2011, **82**, p 934–939

55. C. Maurice and J.H. Driver, High Temperature Plane Strain Compression of Cube Oriented Aluminium Crystals, *Acta Metall. Mater.*, 1993, **41**, p 1653–1664

56. D. Raabe, Texture Simulation for Hot Rolling of Aluminium by Use of a Taylor Model Considering Grain Interactions, *Acta Metall. Mater.*, 1995, **43**, p 1023–1028

57. D. Raabe, Cellular Automata in Materials Science with Particular Reference to Recrystallization Simulation, *Annu. Rev. Mater. Res.*, 2002, **32**, p 53–76

58. D. Raabe and R.C. Becker, Coupling of a Crystal Plasticity Finite-Element Model with a Probabilistic Cellular Automaton for Simulating Primary Static Recrystallization in Aluminium, *Model. Simul. Mater. Sci. Eng.*, 2000, **8**, p 445–462

59. D. Raabe, Z. Zhao, and W. Mao, On the Dependence of In-Grain Subdivision and Deformation Texture of Aluminum on Grain Interaction, *Acta Mater.*, 2002, **50**, p 4379–4394

60. D. Raabe, Z. Zhao, S.J. Park, and F. Roters, Theory of Orientation Gradients in Plastically Strained Crystals, *Acta Mater.*, 2002, **50**, p 421–440

61. F. Roters, P. Eisenlohr, L. Hantcherli, D.D. Tjahjanto, T.R. Bieler, and D. Raabe, Overview of Constitutive Laws, Kinematics, Homogenization and Multiscale Methods in Crystal Plasticity Finite-Element Modeling: Theory, Experiments, Applications, *Acta Mater.*, 2010, **58**, p 1152–1211

62. H. Mirzadeh and A. Najafizadeh, Hot Deformation and Dynamic Recrystallization of 17-4 PH Stainless Steel, *ISIJ Int.*, 2013, **53**, p 680–689

63. D. Samantaray, S. Mandal, C. Phaniraj, and A.K. Bhaduri, Flow Behavior and Microstructural Evolution During Hot Deformation of AISI, Type 316 L(N) Austenitic Stainless Steel, *Mater. Sci. Eng. A*, 2011, **528**, p 8565–8572

64. A. Momeni, K. Dehghani, and G.R. Ebrahimi, Modeling the Initiation of Dynamic Recrystallization Using a Dynamic Recovery Model, *J. Alloy. Compd.*, 2011, **509**, p 9387–9393

65. J. Eickemeyer, D. Selbmann, R. Opitz, B. de Boer, B. Holzapfel, L. Schultz, and U. Miller, Nickel-Refractory Metal Substrate Tapes with High Cube Texture Stability, *Supercond. Sci. Technol.*, 2001, **14**, p 152–159

66. J.H. Driver, D. Juul Jensen, and N. Hansen, Large Strain Deformation Structures in Aluminium Crystals with Rolling Texture Orientations, *Acta Metal. Mater.*, 1994, **42**, p 3105–3114

67. D. Raabe, M. Sachtleber, Z. Zhao, F. Roters, and S. Zaefferer, Micromechanical and Macromechanical Effects in Grain Scale Polycrystal Plasticity Experimentation and Simulation, *Acta Mater.*, 2001, **49**, p 3433–3441

68. M. Sachtleber, Z. Zhao, and D. Raabe, Experimental Investigation of Plastic Grain Interaction, *Mater. Sci. Eng. A*, 2002, **336**, p 81–87

69. C. Zambaldi, F. Roters, D. Raabe, and U. Glatzel, Modeling and Experiments on the Indentation Deformation and Recrystallization of a Single-Crystal Nickel-Base Superalloy, *Mater. Sci. Eng. A*, 2007, **454-455**, p 433–440

70. Z. Zhao, M. Ramesh, and D. Raabe, Investigation of Three-Dimensional Aspects of Grain-Scale Plastic Surface Deformation of an Aluminum Oligocrystal, *Int. J. Plast.*, 2008, **24**, p 2278–2297